# SANDIA REPORT

SAND2014-0190
Unlimited Release
Printed January 2014

# Numerical Modeling of an All Vanadium Redox Flow Battery

Jonathan R. Clausen, Victor E. Brunini, Harry K. Moffat, and Mario J. Martinez

Prepared by
Sandia National Laboratories
Albuquerque, New Mexico 87185 and Livermore, California 94550

Sandia National Laboratories is a multi-program laboratory managed and operated by Sandia Corporation, a wholly owned subsidiary of Lockheed Martin Corporation, for the U.S. Department of Energy's National Nuclear Security Administration under contract DE-AC04-94AL85000.

Approved for public release; further dissemination unlimited.

Sandia National Laboratories

Issued by Sandia National Laboratories, operated for the United States Department of Energy by Sandia Corporation.

**NOTICE:** This report was prepared as an account of work sponsored by an agency of the United States Government. Neither the United States Government, nor any agency thereof, nor any of their employees, nor any of their contractors, subcontractors, or their employees, make any warranty, express or implied, or assume any legal liability or responsibility for the accuracy, completeness, or usefulness of any information, apparatus, product, or process disclosed, or represent that its use would not infringe privately owned rights. Reference herein to any specific commercial product, process, or service by trade name, trademark, manufacturer, or otherwise, does not necessarily constitute or imply its endorsement, recommendation, or favoring by the United States Government, any agency thereof, or any of their contractors or subcontractors. The views and opinions expressed herein do not necessarily state or reflect those of the United States Government, any agency thereof, or any of their contractors.

Printed in the United States of America. This report has been reproduced directly from the best available copy.

Available to DOE and DOE contractors from
U.S. Department of Energy
Office of Scientific and Technical Information
P.O. Box 62
Oak Ridge, TN 37831

Telephone: (865) 576-8401
Facsimile: (865) 576-5728
E-Mail: reports@adonis.osti.gov
Online ordering: http://www.osti.gov/bridge

Available to the public from
U.S. Department of Commerce
National Technical Information Service
5285 Port Royal Rd
Springfield, VA 22161

Telephone: (800) 553-6847
Facsimile: (703) 605-6900
E-Mail: orders@ntis.fedworld.gov
Online ordering: http://www.ntis.gov/help/ordermethods.asp?loc=7-4-0#online

SAND2014-0190
Unlimited Release
Printed January 2014

# Numerical Modeling of an All Vanadium Redox Flow Battery

Jonathan R. Clausen
Fluid Sciences & Engineering
Sandia National Laboratories
P.O. Box 5800
Mail Stop 0828
Albuquerque, NM 87185-0828

Victor E. Brunini
Thermal/Fluid Science and Engineering
Sandia National Laboratories
P.O. Box 969
Mail Stop 9957
Livermore, CA 94551-0969

Harry K. Moffat
Nanoscale & Reactive Processes
Sandia National Laboratories
P.O. Box 5800
Mail Stop 0836
Albuquerque, NM 87185-0836

Mario J. Martinez
Fluid Sciences & Engineering
Sandia National Laboratories
P.O. Box 5800
Mail Stop 0836
Albuquerque, NM 87185-0836

**Abstract**

We develop a capability to simulate reduction-oxidation (redox) flow batteries in the Sierra Multi-Mechanics code base. Specifically, we focus on all-vanadium redox flow batteries; however, the capability is general in implementation and could be adopted to other chemistries. The electrochemical and porous flow models follow those developed in the recent publication by [28]. We review the model implemented in this work and its assumptions, and we show several verification cases including a binary electrolyte, and a battery half-cell. Then, we compare our model implementation with the experimental results shown in [28], with good agreement seen. Next, a sensitivity study is conducted for the major model parameters, which is beneficial in targeting specific features of the redox flow cell for improvement. Lastly, we simulate a three-dimensional version of the flow cell to determine the impact of plenum channels on the performance of the cell. Such channels are frequently seen in experimental designs where the current collector plates are borrowed from fuel cell designs. These designs use a serpentine channel etched into a solid collector plate.

# Acknowledgment

We thank Dr. Imre Gyuk and the Department of Energy for funding this work.

# Contents

**Nomenclature** . . . . . **7**

**1 Introduction** . . . . . **9**

**2 Model Development** . . . . . **12**
2.1 Mathematical Model . . . . . 12
2.2 Figures of Merit . . . . . 17
2.3 Numerical Implementation . . . . . 17

**3 Results** . . . . . **19**
3.1 Binary Electrolyte in Nonparticipating Porous Media . . . . . 19
3.2 Half Cell Verification Problem . . . . . 20
3.3 Full Redox Flow Cell . . . . . 23
3.4 Sensitivity Analysis . . . . . 27
3.5 Impact of Flow Distribution . . . . . 29

**4 Conclusion** . . . . . **37**

**References** . . . . . **38**

# Figures

1 Schematic of a single electrochemical cell for a VRFB. . . . . 12
2 Image in 20 kW VRFB stack design VRB Power, and (b) 260 kW multi-stack installation. Figure from [29]. . . . . 13
3 Binary electrolyte verification results showing (a) expected and simulation potential profiles and (b) convergence of $L_2$ norm demonstrating quadratic convergence for potential field. . . . . 21
4 Half cell used for verification of Butler–Volmer reaction terms. . . . . 21
5 Solid electrode and electrolyte potentials compared with semi-analytic solutions. . . 22
6 A representative coarse mesh used in simulation. For a detailed schematic please see Fig. 1. . . . . 23
7 Cell potential for a full charge and discharge cycle for the vanadium battery. Experimental results are from [28]. . . . . 24
8 Concentration of vanadium ions during the charge cycle showing the reaction (a) products ($c_{II}/c_V$) and (b) reactants ($c_{III}/c_{IV}$) species. The current exchange density, $\nabla \cdot \boldsymbol{i}$, is shown in (c). The flow direction has been scaled to 10% of its original size. 26
9 Power efficiency for the vanadium cell as a function of SOC. . . . . 27
10 Cross section of three-dimensional model employing open channels cut into the collector plates. . . . . 30

11 Distribution of the streamwise component of Darcy velocity across the thickness of the cell for direct electrode injection and for open channel flow injection, with $k_c = 2k_e$ and $k_c = 10k_e$ permeability ($k_e$ is the electrode felt permeability). The profile intersects the middle of an open channel. All curves correspond to the same volumetric flow rate (1 mL-$s^{-1}$) through the full cell. . . . . 32
12 Effect of electrolyte flow configuration on cell potential. . . . . 33
13 Electrolyte concentrations (mol-m$^3$) at 75% SOC during charge for open channel electrolyte injection with 10 $k_e$ channel permeability. In this view, the negative electrode ($c_{II}$ and $c_{III}$) is on the right side, and the positive electrode ($c_{IV}$ and $c_V$) is on the left side. Inflow is from the bottom and outflow at the top. Electrolyte bypassing the porous electrodes via the channels is noted. . . . . 34
14 Electrolyte cross-current density (A-m$^2$) at about 75% SOC during cell charging for (a) direct electrode injection, and open channel injection with (b) $k_c = 2k_e$ and (c) $k_c = 10k_e$ channel permeability. . . . . 35
15 Cross-stream current density (A-m$^2$) on the inflow cross section through the solid conductors, including collector plates and porous felt matrix, during charge for the open channel model with 10K permeability. . . . . 35

# Tables

1 Values for constants used in the binary electrolyte verification problem. . . . . 20
2 Values for constants used in the half-cell electrolyte verification problem. . . . . 22
3 Initial conditions for the full cell validation case corresponding to the data in [28]. All concentrations in mol-m$^{-3}$ . . . . . 23
4 Parameters used in the full redox flow battery case . . . . . 25
5 Means and standard deviations used for sensitivity sampling procedure. All distributions are log-normal. . . . . 28
6 Sensitivities of average charge voltage, average discharge voltage, and cycle voltage efficiency on each sampled property. Sensitivities are total Sobol indices. . . . . 29
7 Flow pressures for 10 cm flow length . . . . . 31

# Nomenclature

**SOC** State of Charge

**RFB** Redox Flow Battery

**VRFB** Vanadium Redox Flow Battery

$A$ Specific surface area of carbon electrode

$c_i$ Concentration of species $i$

$c_i^s$ Concentration of species $i$ at the electrode surface

$D_i$ Diffusion coefficient for species $i$

$d_f^2$ Mean fiber diameter

$E'_{0,k}$ Equilibrium potential associated with reaction $k$

$F$ Faraday's constant

$\boldsymbol{i}$ Current

$i_{0,k}$ Current exchange density for reaction $k$

$K$ Kozeny–Carman constant for a fibrous media

$k_p$ Hydraulic permeability of the membrane

$k_\phi$ Electrokinetic permeability of the membrane

$k_e$ Hydraulic permeability of the electrode

$k_c$ Hydraulic permeability of the flow channel

$\boldsymbol{N}_i$ Superficial flux of species $i$

$p$ Pressure

$S_i$ Source of species $i$

$R$ Universal gas constant

$T$ Temperature

$t$ Time

$\boldsymbol{v}$ Velocity

$V(\cdot)$ Vanadium and associated oxidation level

$z_i$ Valence of species $i$

$\alpha_{+/-}$ Transfer coefficient

$\gamma_l$ Fitting parameter for Butler–Volmer reaction form

$\epsilon$ Porosity

$\eta$ Overpotential

$\kappa_{eff}$ Effective ion conductivity

$\mu$ Viscosity

$\sigma_{col}$ Electrical conductivity of collector plate

$\sigma_s^{eff}$ Electrical conductivity of porous electrode

$\phi$ Potential

$\phi_{cell}$ Overall cell potential

$\phi_e$ Potential in electrolyte

$\phi_s$ Potential in solid phase of porous electrode

$\eta_k$ Overpotential associated with reaction $k$

# 1 Introduction

Increasingly, there is a desire to transition away from traditional fossil-fuel and nuclear based energy sources and towards more sustainable and renewable sources of energy such as wind and solar. Unfortunately, these resources are inherently intermittent in supply. In its current form, the U.S. energy grid is nearly devoid of any energy storage, and all electrical energy used must be generated on demand. This lack of storage poses considerable problems when coupled with the intermittent nature of renewable energy sources. Recently, analysis has suggested that increasing the relative portfolio of renewable energy resources to 20% will create electrical grid destabilization [25]. Consequently, grid-scale energy storage technologies are needed to mitigate these issues.

One particular technology that appears poised to offer a solution to grid-scale energy storage needs is the redox flow battery (RFB). Unlike traditional batteries, which typically use solid electrodes for the oxidation and reduction reactions, RFBs rely on solution-based redox species. These redox solutions are stored externally in tanks, and the solutions are pumped through an inert electrode stack where the redox reactions occur at the surface of the electrodes. The species associated with the anode and cathode reactions are separated by an ion selective membrane. Typical materials for the electrode are graphite or carbon felt/paper. These reactions are reversible, which allows for high efficiencies. Although many different chemistries are available for flow batteries, one of the most promising for commercialization is the all vanadium RFB (VRFB). For an extensive review of RFBs and alternate chemistries see [9, 29, 43] as well as recent work for non-aqueous-based chemistries [42]. The all vanadium chemistry assures that any undesirable transfer of vanadium through the ion exchange membrane will not permanently impair the performance of the battery, although it will temporarily decrease the cycle efficiency [37, 30, 18]. In addition to grid energy storage and associated load-leveling operations, RFBs have been used in emergency backup operations in lieu of traditional lead-acid batteries and generators for remote power applications [29]. Several attributes contribute to the desirability of RFBs, and VRFBs in particular, for the application to grid-energy storage and load-leveling operations:

1. High energy efficiencies are attainable (85–90% [9, 10, 29]). These efficiencies compare favorably with traditional flooded lead-acid batteries with an efficiency of 70–80% [9].

2. Energy storage capacity is dictated by the amount of redox species in solution. Thus, capacity can be increased to meet requirements by increasing the size of the storage tanks independent of the electrode stack size and design parameters. Similarly the system power requirements are met independently by the electrode stack design.

3. Traditional battery technologies can degrade due to changes in electrode morphology caused by phase changes associated with the solid-state electrochemical reactions. Since the redox species are entirely in solution, electrode fouling issues are mitigated, and VRFBs typically enjoy large cycle life compared with traditional battery technologies. Also, partial cycling and deep cycling are not detrimental to VRFBs. Estimated lifespans are on the order of 1000 cycles for traditional lead-acid batteries and order 10,000 cycles for VRFBs [10]. VRFBs also show negligible self discharge compared with 2–5% per month for lead-acid batteries [10].

4. VRFBs do not depend on specific geological or topographical features, unlike compressed-air storage or pumped hydroelectric.

5. VRFBs have response times on the order of milliseconds, which allows the cells to respond to rapidly fluctuating power demands [9, 29].

The pioneering research for VRFBs was performed in the 1980s, where systems using graphite plates were investigated experimentally [33, 34, 31]. Research has progressed rapidly with electrode developments including using carbon felt [17] and thermally treating the felt to create surface functional groups [36, 35]. Also, extensive research is ongoing regarding the membrane construction, since the performance and longevity of the battery is in part dictated by the ion exchange membrane, and efficiency can be improved by reducing membrane permeability to vanadium while maintaining high ionic conductivity. Existing designs rely heavily on Nafion, which is expensive, although other chemistries are being investigated [44, 16, 12]. A detailed timeline of major developments can be found in [29].

Modeling efforts for these systems have somewhat lagged the experimental investigations; however, a rapid increase in interest and commensurate publications can be seen over the past decade. The earliest modeling efforts were transient zero-dimensional models [19]. Work quickly expanded to two-dimensional models [28], which focused on studying the effects of inlet concentration, flow rate, and porosity. This model was refined to account for oxygen evolution [4, 27, 3]. Additional modeling efforts have been undertaken to predict effects of applied current density [46], three-dimensional effects [22], analysis of electrode stacks [41], membrane geometry [1, 21], and ion cross contamination [37, 30, 18].

Successful commercial installations of VRFBs can be found from VRB Power Systems and Sumitomo Electric Industries/Kansai Electric. Current examples include a 275 kW output balancer in use on a wind power project in the Tomari Wind Hills of Hokkaido, Japan; a 200 kW, 800 kWh output leveller in use at the Huxley Hill Wind Farm on King Island, Tasmania; a 250 kW, 2 MWh load leveller in use at Castle Valley, Utah; and two 5 kW units installed at Safaricom GSM site in Katangi and Njabini, Winafrique Technologies, Kenya. See the all-vanadium section in [29] for another good description of successful installations.

Despite some success, issues remain with the VRFB technology, and more research and modeling efforts are necessary for VRFBs to become a commercially viable energy storage tool. Improvements needed include improving energy density, reducing self-discharge, improving stack flow distribution, and improving membrane performance, reducing membrane cross-over of electrolytes and water, lowering cost, improving safety, and improving battery lifetime. DOE and industry reports indicate flow battery modeling as an important part of the research needed to advance the technology [38, 39]. Some open issues that could benefit from additional modeling include the following: Describing the cross contamination of vanadium species and its tendency to reduce capacity after high cycle counts [18], increasing the relatively poor energy-to-volume ratio [41], improving the predicted cell voltage [18], and exploring design issues such as self-discharge, shunt (leakage) currents, self discharge, contact electrical resistances, flow distribution and pumping losses, back mixing, and compensating for water transport across the membrane via osmotic pressure differences (see discussion in review article by [9]).

In this work, we discuss the development and application of a general-purpose numerical model for understanding and improving redox flow batteries. The goal is to provide designers of flow cells a high-performing low-cost modeling tool to optimize their flow battery designs. This paper proceeds by describing in detail the models used, and overviews their implementation in a finite-element framework in Section 2. Next, several small verification problems are studied including a binary electrolyte, and a redox half cell with constrained concentrations. Then, the experimental results presented in [28] are compared with the implemented model (also from [28]) in Section 3.3. Next a sensitivity study on many of the model parameters is performed. Lastly, a three-dimensional version of the electrode stack is considered in which channels are used to provide an easier path for electrolyte flow in Section 3.5.

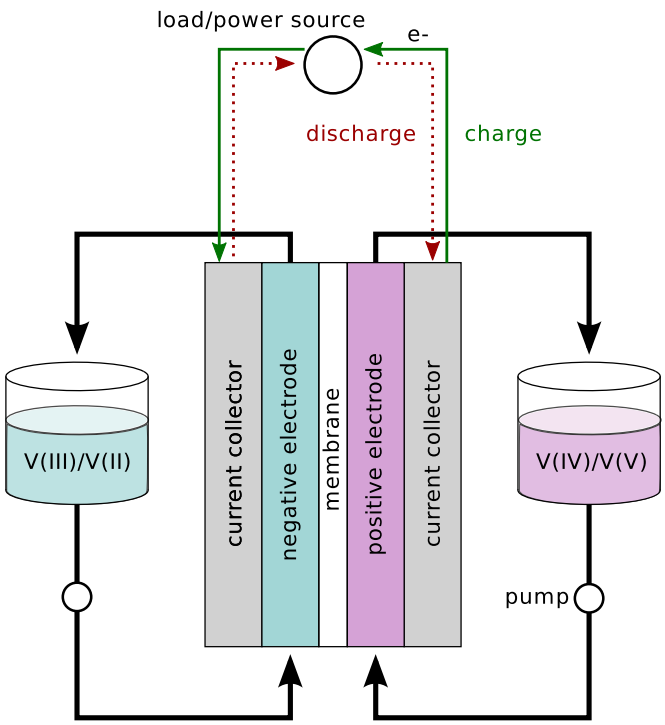


**Figure 1.** Schematic of a single electrochemical cell for a VRFB.

# 2 Model Development

A single anode/cathode electrode pair forms the basic building block of VRFB installations. As discussed in the introduction, the electrodes are composed of nonreactive substances (typically carbon felt or paper) which are separated by a selective ion exchange membrane. Redox species are stored externally in tanks. A basic cell schematic is shown in Fig. 1.

Typically, a VRFB installation consists of bipolar stacks of electrodes in order to increase the operating voltage and power capacity. For example, Huamin and co-workers at the Dalian Institute of Chemical Physics and Rongke Power Co., Ltd in China have designed a 20kW stack model [29]. A single stack is shown in Fig 2(a), with an installation of stacks in a 260 kW subsystem shown in Fig. 2(b).

## 2.1 Mathematical Model

We largely follow the mathematical model developed by [28]. Our primary goal is an initial modeling capability for flow batteries, with the plan that additional physics would be added as needed to improve the fidelity of the model. Current limitations include a simple, one step description of

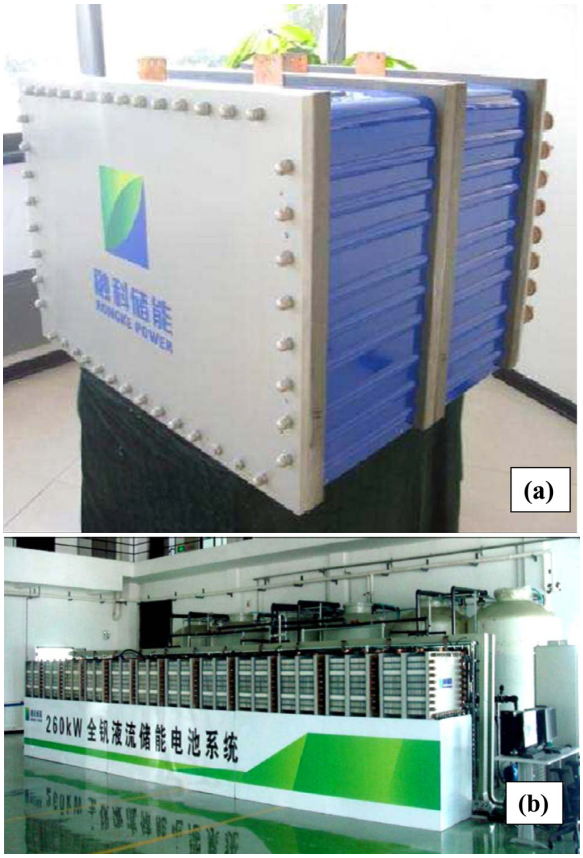


**Figure 2.** Image in 20 kW VRFB stack design VRB Power, and (b) 260 kW multi-stack installation. Figure from [29].

the vanadium half reactions with no parasitic reactions, no tracking of water migration through the membrane, and no tank models for storing the electrolyte. The primary half reactions involved in the Vanadium Redox Flow Battery (VRFB) are

$$V(III) + e^- \rightleftharpoons V(II), \tag{1}$$

$$\underbrace{VO^{2+}}_{V(IV)} + H_2O \rightleftharpoons \underbrace{VO_2^+}_{V(V)} + 2H^+ + e^-, \tag{2}$$

where the half reactions above are referred to in subsequent equations as reactions $k = 1, 2$, respectively. The following side reactions are also known to be present

$$2H_2O + 2e^- \rightleftharpoons H_2 + 2OH^-, \tag{3}$$

$$2H_2O \rightleftharpoons O_2 + 4e^- + 4H^+, \tag{4}$$

$$VO^{2+} + 2H_2O \rightleftharpoons HVO_3 + 3H^+ + e^-, \tag{5}$$

but they are excluded from this numerical model. In reality, the kinetics of the side reactions are complex and to a large degree unknown [11, 14].

Ion species migration in the porous electrodes is governed with a mass concentration conservation equation,

$$\frac{\partial(\epsilon c_i)}{\partial t} + \nabla \cdot \boldsymbol{N}_i = -S_i, \tag{6}$$

where $\epsilon$ is the local porosity, $\boldsymbol{N}_i$ is the superficial flux of species $i$ and $S_i$ is a species source term driven by the electrochemical reactions. The species flux is composed of three sources: molecular diffusion, a migration term caused by gradients in the potential, and advection. These terms are modeled using the Nernst–Planck relationship valid for dilute concentrations [23],

$$\boldsymbol{N}_i = -D_i^{eff} \nabla c_i - \frac{z_i c_i D_i^{eff}}{RT} F \nabla \phi_e + \boldsymbol{v} c_i, \tag{7}$$

where $z_i$ is the species valence, $c_i$ is the molar concentration of the $i^{th}$ species, $F$ is Faraday's constant, $R$ is the universal gas constant, $T$ is the temperature, and $\phi_e$ is the potential in the electrolyte. Throughout this manuscript, subscripts $e$, $s$, and $m$ refer to the electrolyte, solid, and membrane, respectively. The effective diffusivity of the ions is given by a Bruggeman correction to the molecular diffusivity,

$$D_i^{eff} = \epsilon^{3/2} D_i. \tag{8}$$

The superficial macroscopic velocity $\boldsymbol{v}$ is governed by Darcy's law, in which a Kozeny-Carmen law is used for the hydraulic conductivity in the porous felt

$$\boldsymbol{v} = -\frac{d_f^2}{K\mu} \frac{\epsilon^3}{(1-\epsilon^2)} \nabla p, \tag{9}$$

where $d_f$ is the porous felt fiber diameter, $K$ is the Kozeny–Carman constant, $\mu$ is the dynamic viscosity of the fluid, and $p$ is the pressure. In all cases we assume dilute concentration theory, and we treat mass- and molar-averaged velocities as approximately equal.

Darcy's law is combined with the condition of continuity for an incompressible liquid,

$$\nabla \cdot \boldsymbol{v} = 0, \tag{10}$$

giving an equation with pressure as the unknown variable.

The transfer of charge between the porous carbon felt (the electrode) and the electrolyte occurs at the surface of the carbon fiber. This transfer is averaged over a representative volume element in the porous flow assumption [23], and the conservation of charge dictates that

$$\nabla \cdot \boldsymbol{i} = \nabla \cdot \boldsymbol{i}_e + \nabla \cdot \boldsymbol{i}_s = 0, \tag{11}$$

where $\boldsymbol{i}$ is the current. In the electrolyte, current transport occurs solely through the migration of ions, where

$$\boldsymbol{i}_e = \sum_i z_i F \boldsymbol{N}_i. \tag{12}$$

Additionally, to a very good approximation electroneutrality holds, i.e.,

$$\sum_i z_i c_i = 0. \tag{13}$$

Substituting (7) into (12) and using (13) results in an expression for the current density in the electrolyte,

$$\boldsymbol{i}_e = \sum_i \boldsymbol{i}_i = -\kappa^{eff} \nabla \phi - F \sum_i z_i D_i^{eff} \nabla c_i, \tag{14}$$

where the effective ionic conductivity $\kappa^{eff}$ is given by

$$\kappa^{eff} = \frac{F^2}{RT} \sum_i z_i^2 D_i^{eff} c_i. \tag{15}$$

In the solid matrix of the porous electrode, the current distribution is governed by Ohm's law,

$$\boldsymbol{i}_s = -\sigma_s^{eff} \nabla \phi_s, \tag{16}$$

where $-\sigma_s^{eff}$ is the effective electrical conductivity of the porous felt, which given by a Bruggeman correction

$$\sigma_s^{eff} = (1 - \epsilon)^{3/2} \sigma_s. \tag{17}$$

The reaction kinetics are modeled using a simplified Butler–Volmer form, resulting the following expression for the current transfer density,

$$\nabla \cdot \boldsymbol{i}_e = i_{0,k} \left\{ \exp\left( \frac{\alpha_{+,k} F \eta_k}{RT} \right) - \exp\left( -\frac{\alpha_{-,k} F \eta_k}{RT} \right) \right\}, \tag{18}$$

where $i_0$ is the current exchange density, defined for reactions 1 and 2 as

$$i_{0,1} = \gamma_l \left(c_{III}^s\right)^{\alpha_{-,1}} \left(c_{II}^s\right)^{\alpha_{+,1}} A F k_1 \tag{19}$$

$$i_{0,2} = \gamma_l \left(c_{IV}^s\right)^{\alpha_{-,2}} \left(c_{V}^s\right)^{\alpha_{+,2}} A F k_2. \tag{20}$$

Here, $A$ is the specific surface area of the porous electrode, $\alpha_{+/-}$ refer to the cathodic and anodic charge transfer coefficients, $\gamma_l$ is a fitting parameter, and $k_{1,2}$ are the kinetic rate constants. The overpotential is defined as

$$\eta_k = \phi_s - \phi_e - E_{0,k}, \tag{21}$$

where $k$ refers to half reactions 1 and 2. The open circuit equilibrium potentials for reactions 1 and 2 are given according to the Nernst equations,

$$E_{0,1} = E_{0,1}^{'} + \frac{RT}{F} \ln\left(\frac{c_{III}^s}{c_{II}^s}\right), \tag{22}$$

$$E_{0,2} = E_{0,2}^{'} + \frac{RT}{F} \ln\left(\frac{c_{V}^s}{c_{IV}^s}\right), \tag{23}$$

where $E_{0,k}^{'}$ is the equilibrium Nernst potential and $c_i^s$ is the molar concentration of species $i$ at the electrode surface.

As noted, there are numerous side reactions present, but the essential nature is well captured by the reversible single step reactions shown in (1) and (2) [19]. Also, the concentrations present are surface concentrations, i.e., the species concentration just outside the double layer. A one-dimensional model has been used to approximate the surface concentration in the pore space by balancing the reaction rate with species diffusion over the length scale of the pore [28]; however, we find that this model does not significantly affect the full system model and is neglected unless otherwise noted. Full expressions relating the surface concentration to the bulk concentration can be found in [28].

In the membrane, charge is carried by the transport of protons through the membrane, which is modeled using the Bernardi and Verbrugge formulations [6, 7]. The velocity of water transported through the membrane is governed by Schloegl's equation,

$$\boldsymbol{v} = -\frac{k_\phi}{\mu_{H_2O}} F c_{H^+} \nabla \phi_m - \frac{k_p}{\mu_{H_2O}} \nabla p, \tag{24}$$

where $k_\phi$ is the electrokinetic permeability, $k_p$ is the hydraulic permeability, $\mu_{H_2O}$ is the viscosity of water, $\phi_m$ is the potential in the membrane, and $c_{H^+}$ is the proton concentration. The proton concentration is a fixed quantity related to the density of the fixed charge sites in the membrane structure, e.g., sulfonic acid groups in Nafion membranes. Current density is related to gradients in ionic potential,

$$0 = \nabla \cdot \boldsymbol{i}_e = \nabla \cdot \boldsymbol{N}_{H^+} = -\frac{F^2}{RT} D_{H^+,m}^{eff} \nabla^2 \phi_m, \tag{25}$$

where $D_{H^+,m}^{eff}$ is the effective diffusivity of protons in the membrane. The pressure distribution is calculated by assuming continuity, yielding

$$-\frac{k_p}{\mu_{H_2O}} \nabla^2 p = 0 \tag{26}$$

after eliminating terms involving potential using (25). While we do couple the pressure field through the membrane, the quantity of water transfered is not tracked in our tank model and does not affect the species concentrations. Current transport in the current collectors is governed by a Ohm's law with $\sigma_{col}$ as the electric conductivity.

## 2.2 Figures of Merit

The performance of a redox flow cell can be quantified using several efficiencies [9]. The voltage efficiency is the ratio of cell voltages between charge and discharge

$$\eta_V = \frac{\phi_{cell}(discharge)}{\phi_{cell}(charge)}, \tag{27}$$

where the charge and discharge cell voltages ($\phi_{cell}$) correspond to a specific time or state of charge. Another efficiency metric is the charge efficiency (also known as Faraday or Coulombic efficiency), which is the ratio of total electrical charge during discharge compared with charge,

$$\eta_C = \frac{Q(discharge)}{Q(charge)}, \tag{28}$$

where $Q$ refers to the total electrical charge over a cycle. Other performance metrics are the energy efficiency

$$\eta_e = \frac{E(discharge)}{E(charge)}, \tag{29}$$

where $E$ is the measure of total energy, and the power efficiency

$$\eta_p = \frac{I\phi_{cell}(discharge)}{I\phi_{cell}(charge)}, \tag{30}$$

where $I$ is the total current into the cell.

## 2.3 Numerical Implementation

The equations outlined in the previous section constitute a complex set of equations whose numerical solution is not trivial. In contrast to previous works [28, 4, 3, 27], the system is not modeled using commercial software, nor are pre-built modules supplied by a vendor. This section will outline the finite element numerical technique used to simulate the model described in Section 2. The model equations are discretized using finite elements within the Sierra multiphysics framework [24]. The Sierra multiphysics suite allows the inclusion of tightly coupled, complex physical models with full-Newton sensitivities for a generalized Newton nonlinear solution technique. Also, Sierra uses Trilinos [15] to offer a wide variety of linear system preconditioners and solvers.

The porous flow equation, the porous species equations, and the current equation are solved using a standard Galerkin method using bilinear quadrilateral elements. Standard Galerkin discretizations are known to perform well for diffusion dominated problems, as is generally the case for the flow battery simulations shown here. For more convection-dominated flows, some form of upwinding stabilization is needed (e.g., streamline-upwind Petrov Galerkin [8]). Also, the pure Galerkin method does not satisfy a discrete maximum principle, thus negative concentrations can occur and need to be handled appropriately. Initially, the Nernst forms (22-23) for the overpotential appear problematic around zero surface concentrations; however, when combined with the

Butler–Volmer form (18), one can show that the current exchange density is linear in the surface concentrations. It is important to implement this form in the code.

Solution of the full flow battery system is solved using a GMRES solver, with a Schwartz domain decomposition preconditioner based on incomplete factorization. We also noted a performance improvement by perturbing the diagonal of the system. The tank models were not implemented explicitly at this state of modeling; however, the reactions shown in Section 3 are 100% charge efficient, thus the inlet concentration flux can be calculated exactly based on a stoichiometric balance of species produced and the integrated current flux applied. Obviously, a fully mixed tank model would be needed before considering side chemical reactions because the system would no longer exhibit 100% charge efficiency.

# 3 Results

We present numerical results obtained by simulating the described model using a finite element discretization in the SIERRA multiphysics simulation code. The first two results compare the simulated results with known analytical or semianalytical results. Next, we compare simulation results of a full-scale flow battery with the experimental results detailed in [28]. In order to provide some guidance for future flow battery designs, we perform a sensitivity study on the parameters in the full flow battery model. Lastly, we explore alternative design geometries by simulating a three-dimensional system that includes free-flowing channels.

## 3.1 Binary Electrolyte in Nonparticipating Porous Media

To verify the correct behavior of the Nernst ionic migration term (7), we simulate a simple binary electrolyte flowing through a nonparticipating porous media. This problem consists of an inert (non-conductive and non-reactive) porous media that contains the binary electrolyte. At either end of the porous structure there are collector plates. This problem is similar to the single-phase binary electrolyte, and analytical solutions are readily available (for solution methodology, see [23]). For this problem, consider two fictitious ions formed from the disassociation of a salt, with concentrations $c_+$ and $c_-$. Electroneutrality requires that $c_+/\nu_+ = c_-/\nu_- = c$, where $\nu$ is the number of cations and anions produced by the dissolution of one molecule of salt.

In this case, a constant current is applied across the one-dimensional simulation domain. We assume that a source of positive ions exists from the dissolution of the current collector on one side, and a sink of positive ions exists on the other from the ions plating out of solution. There exists a constant flux of $c_+$ ions, while there is no flux of $c_-$ ions. A common example of this system is $CuSO_4$, where $Cu^{2+}$ ions migrate from one copper collector plate to another while the $SO_4^{2-}$ ions demonstrate no flux.

By eliminating the potential for the fluxes of cations and anions, the steady-state concentration for the above case can be written as

$$c = -\frac{1 - t_+}{D}\frac{i}{z_+\nu_+F}x + c_0, \tag{31}$$

where $c_0$ is an arbitrary constant determined by the initial concentration, and $x$ is the coordinate. The cation transference number is defined as

$$t_+ = 1 - t_- = \frac{z_+u_+}{z_+u_+ - z_-u_-}, \tag{32}$$

where $u_i = D_i/RT$ is the mobility. $D$ is an average diffusivity calculated according to

$$D = \frac{z_+u_+D_- - z_-u_-D_+}{z_+u_+ - z_-u_-}, \tag{33}$$

The potential distribution is solved according to (7) using the known concentration and particle flux, and assuming quiescent conditions for the velocity. For the fictitious values shown in Table 1,

**Table 1.** Values for constants used in the binary electrolyte verification problem.

| Variable | Value |
|---|---|
| $\nu_+, \nu_-$ | 1 |
| $z_+$ | 2 |
| $z_-$ | −2 |
| $t_+$ | 0.6 |
| $c_0$ | $1,000$ mol-m$^{-2}$ |
| $i$ | 100 A-m$^{-2}$ |
| $D$ | $1.0 \times 10^{-10}$ m-s$^{-2}$ |
| $\phi_{bc}$ | 0.0 V |
| $T$ | 300 K |

the expected and simulated concentration and potential values are shown in Fig. 3(a). Excellent agreement is seen between analytical and simulation. Plotting the $L_2$ norms of the error shows quadratic convergence, shown in Fig. 3(b). This behavior is expected, since the finite element method is second-order accurate.

## 3.2 Half Cell Verification Problem

To verify the proper behavior of the porous Butler–Volmer reaction terms, a half cell is simulated with a fixed uniform concentration profile. This half cell corresponds to the negative electrode in [28], and the initial concentrations for the vanadium species $V_{II}$ and $V_{III}$ are chosen to be constant values of 27.0 and 1053.0 mol-m$^{-3}$, respectively. Other ion concentrations are $HSO_4^-$ = 1200.0 mol-m$^{-3}$, $SO_4^{2-}$ = 1606.5 mol-m$^{-3}$, and $H^+$, which is determined from electroneutrality. The half cell is schematically shown in Fig. 4. The current flux is described as a flux of $H^+$ ions entering the domain on the right from the membrane, and on the left directly as a current flux on the potential equation. Using the governing equations outlined in section 2, the potential distribution can be described analytically using the following ODE system

$$\kappa^{eff}\phi_e'' = \alpha\left\{\exp\left[\beta\left(\phi_s - \phi_e - U\right)\right] - \exp\left[-\beta\left(\phi_s - \phi_e - U\right)\right]\right\} \tag{34}$$

$$\sigma^{eff}\phi_s'' = -\alpha\left\{\exp\left[\beta\left(\phi_s - \phi_e - U\right)\right] - \exp\left[-\beta\left(\phi_s - \phi_e - U\right)\right]\right\} \tag{35}$$

where $\beta \equiv F/2RT = 19.3$, $\alpha \equiv AFk_1\sqrt{c_{VII}c_{VIII}} = 3.87 \times 10^6$, $\kappa^{eff} = 2522.2$, and $\sigma^{eff} = 90.5$. Other parameters used in this simulation are shown in Table 2. This system is solved numerically in using a simple boundary-value integration scheme (bvp4c in Matlab). The results are shown in Fig. 5, with good agreement seen between the finite element simulation and the semianalytical result.

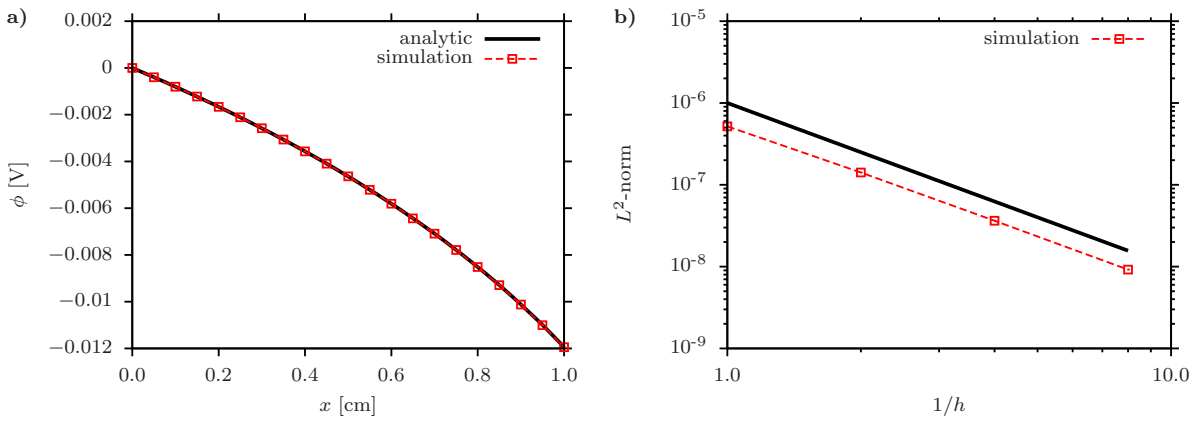


**Figure 3.** Binary electrolyte verification results showing (a) expected and simulation potential profiles and (b) convergence of $L_2$ norm demonstrating quadratic convergence for potential field.

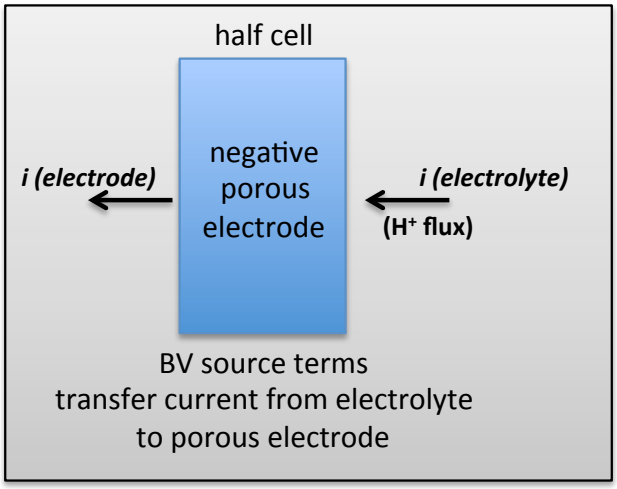


**Figure 4.** Half cell used for verification of Butler–Volmer reaction terms.

**Table 2.** Values for constants used in the half-cell electrolyte verification problem.

| Variable | Value |
|---|---|
| $c_{VII}$ | 27 mol-m$^{-3}$ |
| $c_{VIII}$ | 1053 mol-m$^{-3}$ |
| $i$ | 1000 A-m$^{-2}$ |
| $\phi_{bc}$ | 0.0 V |
| $T$ | 300 K |
| $\epsilon$ | 0.68 |
| $k$ | $1.75 \times 10^{-7}$ |
| $i_0$ | 22963.0 A-m$^{-2}$ |
| $\alpha_{+/-}$ | 0.5 |

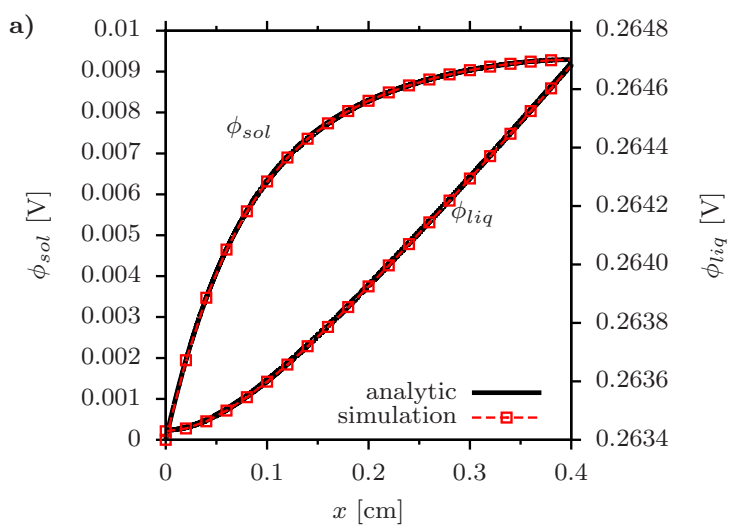


**Figure 5.** Solid electrode and electrolyte potentials compared with semi-analytic solutions.

**Table 3.** Initial conditions for the full cell validation case corresponding to the data in [28]. All concentrations in mol-m$^{-3}$

| Species | $c_0$ = 1080 | $c_0$ = 1440 |
|---|---|---|
| $c_{II}$ | 27 | 36 |
| $c_{III}$ | 1053 | 1404 |
| $c_{IV}$ | 1053 | 1404 |
| $c_V$ | 27 | 36 |
| $c_{HSO_4}$ | 1200 | 1200 |
| $c_{H_p}$ | 1200 | 1200 |

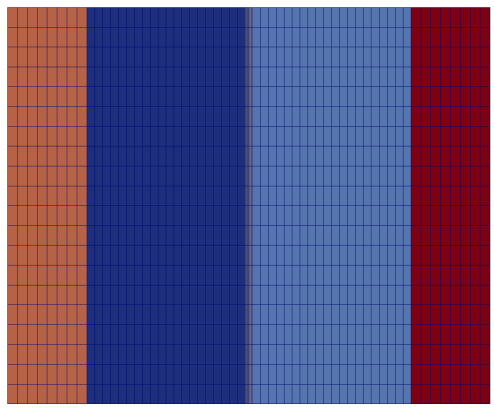

**Figure 6.** A representative coarse mesh used in simulation. For a detailed schematic please see Fig. 1.

## 3.3 Full Redox Flow Cell

The full system shown in Fig. 1 is simulated through a charge–discharge cycle. Some ambiguity exists regarding the initial conditions presented in [28]. The text refers to an initial condition of $c_{III}$ equal to 1080 or 1440 mol-m$^{-3}$; however, the tabular initial condition data (cf. figure 2) refer to a total vanadium load of 1080 mol-m$^{-3}$. Initial concentrations of $c_{II}$ and $c_V$, the products during the charge cycle, are not given outside of the tabular data, and are only given for the 1080 mol-m$^{-3}$ case. Thus, we choose to simulate the system for two initial prescribed inlet condition states with *total* vanadium loads, $c_0$, of 1080 and 1440 mol-m$^{-3}$ at a given state of charge (SOC) of 2.5%. The initial conditions for both cases are shown in Table 3. Concentrations of $SO_4^{2+}$ are determined via electroneutrality.

A current flux density of 1000 A-m$^{-2}$ is applied at the right (positive) collector (see Fig. 1 and Fig. 6), which corresponds to a total current of 10 A. Dirichlet zero potential is prescribed at the left (negative) collector. Inlet conditions are a specified flow rate of 1 mL-s$^{-1}$ for each electrode. With no parasitic reactions or water migration, the inlet concentration can be approximated by

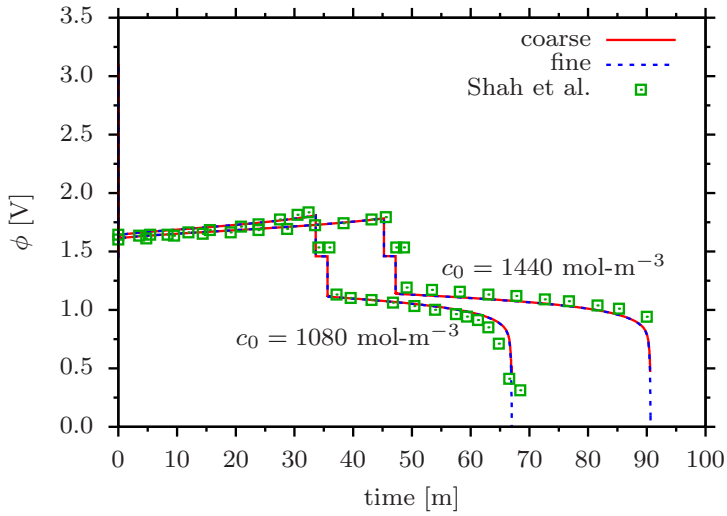


**Figure 7.** Cell potential for a full charge and discharge cycle for the vanadium battery. Experimental results are from [28].

adjusting the inlet concentrations according to the total current flux introduced to the cell, i.e., every electron introduced via an applied current flux must give rise to the conversion of vanadium species throughout the system, including a tank. The equation is written as

$$c(t) = \frac{(\pm)I}{V_T F} t + c(t = 0) \tag{36}$$

where $(\pm)I$ represents the current flux with the appropriate sign chosen based on whether the concentration in question is a product or reactant. The outlet flow condition is open flow. The membrane is set to a fixed $c_{H^+}$ based on the number of fixed sulfinate charge sites, with the potential distribution in the membrane calculated by (25). Membrane permeability is accounted for in the pressure field; however, the flux of water between positive and negative electrodes is not included in the tank model, i.e., it has no effect on the concentrations. The current collector plates are modeled as equipotential surfaces, which is approximated by a high conductivity ($1.0 \times 10^8$ S-m$^{-1}$). A full range of parameters can be found in Table 4. No shunt or leakage currents are considered, i.e., no current flux is prescribed at the inlet and outlet.

To validate the model, we compare our results with the experimental results published in [28] for a full charge discharge cycle at each vanadium loading, as shown in Fig. 7. For the low concentration case, charge commences until 33.6 min, which is followed a period of 2 min of zero current draw, and finally discharge to approximately 65 min. For the high-concentration case, charge commences until 45.2 min, followed by 2 min of zero current, and discharge until approximately 90 min. Since our model is based on that of [28], agreement is seen with the experimental results, as expected. Two mesh resolutions are modeled, with negligible differences seen. The concentrations of vanadium ions are shown in Figs. 8(a and b) during charge of the low concentration system at a time of 11.0 min (~25% SOC). Observe the large concentration gradients near

**Table 4.** Parameters used in the full redox flow battery case

| Variable | Description | Value |
|---|---|---|
| $h_e$ | Electrode heigh (cm) | 10 |
| $t_e$ | Electrode thickness (mm) | 4 |
| $w_e$ | Electrode width (cm) | 10 |
| $t_m$ | Membrane thickness (μm) | 180 |
| $\epsilon$ | Electrode porosity [28] | 0.68 |
| $\sigma_s$ | Solid conductivity of porous electrode (S-m$^{-1}$) | 500.0 |
| $d_f$ | Fiber diameter [28] (μm) | 10 |
| $V_T$ | Electrolyte volume (per half cell) (mL) | 277 |
| $A_e$ | Specific surface area of electrode [28] (m$^{-1}$) | $2.0 \times 10^6$ |
| $\gamma_l$ | Current exchange density fitting parameter | 0.0375 |
| $k_1$ | Reaction rate for negative electrode [28] (m-s$^{-1}$) | $1.75 \times 10^{-7}$ |
| $k_2$ | Reaction rate for positive electrode [14] (m-s$^{-1}$) | $3.0 \times 10^{-9}$ |
| $\alpha_{+/-,i}$ | Transfer coefficient (anode and cathode) for reactions 1 and 2 | 0.5 |
| $E'_{0,1}$ | Equilibrium potential for reaction 1 [26] (V) | −0.255 |
| $E'_{0,2}$ | Equilibrium potential for reaction 2 [26] (V) | 1.004 |
| $c_f$ | Membrane fixed sulfonate charge [6] (mol-m$^{-3}$) | 1200 |
| $D_{II}$ | Diffusivity of V(II) in electrolyte [45] (m$^2$-s$^{-1}$) | $2.4 \times 10^{-10}$ |
| $D_{III}$ | Diffusivity of V(III) in electrolyte [45] (m$^2$-s$^{-1}$) | $2.4 \times 10^{-10}$ |
| $D_{IV}$ | Diffusivity of V(IV) in electrolyte [45] (m$^2$-s$^{-1}$) | $3.9 \times 10^{-10}$ |
| $D_V$ | Diffusivity of V(V) in electrolyte [45] (m$^2$-s$^{-1}$) | $3.9 \times 10^{-10}$ |
| $D_{H^+}$ | Diffusivity of $H^+$ in electrolyte [20] (m$^2$-s$^{-1}$) | $9.31 \times 10^{-9}$ |
| $D_{HSO_4^-}$ | Diffusivity of $HSO_4^-$ in electrolyte [47] (m$^2$-s$^{-1}$) | $1.23 \times 10^{-9}$ |
| $D_{SO_4^{2-}}$ | Diffusivity of $SO_4^{2-}$ in electrolyte [47] (m$^2$-s$^{-1}$) | $2.2 \times 10^{-10}$ |
| $D^{eff}_{H^+,m}$ | Effective diffusivity of $H^+$ in membrane [40] (m$^2$-s$^{-1}$) | $1.4 \times 10^{-9}$ |
| $K$ | Kozeny–Carman constant in porous electrode [28] | 5.55 |
| $k_\phi$ | Electrokinetic permeability in the membrane [40] (m$^2$) | $1.13 \times 10^{-19}$ |
| $k_p$ | Hydraulic permeability in the membrane [28] (m$^2$) | $1.58 \times 10^{-19}$ |
| $\mu_{H_20}$ | Water viscosity (Pa-s) | $10^{-3}$ |

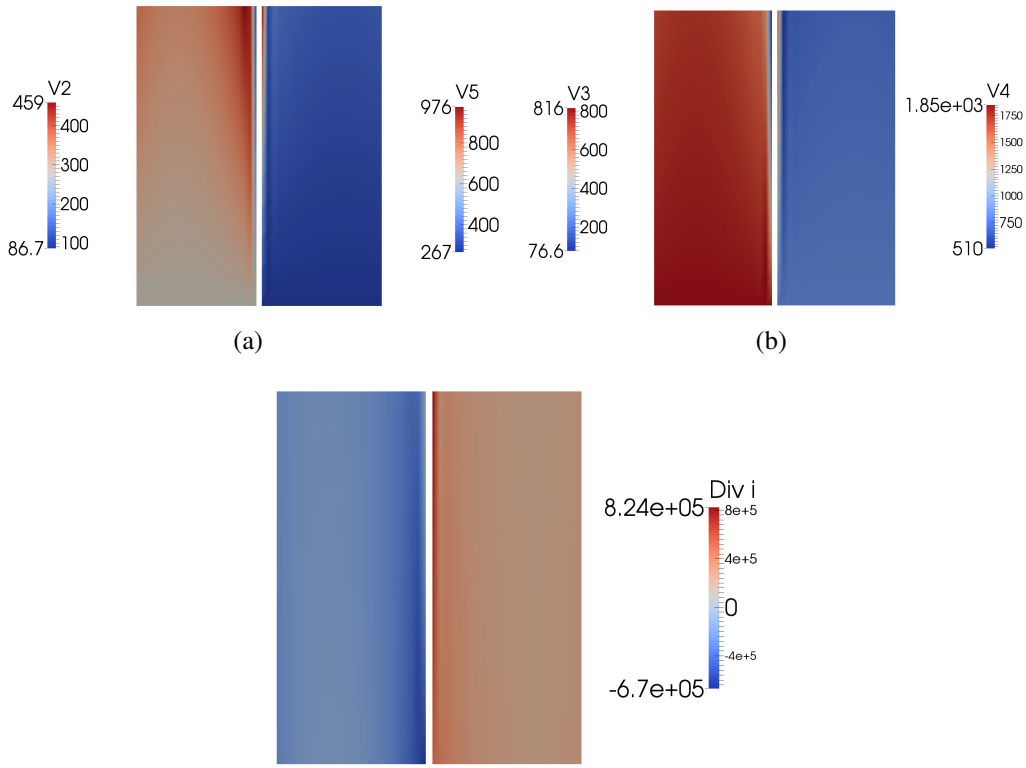


(a) (b)

(c)

**Figure 8.** Concentration of vanadium ions during the charge cycle showing the reaction (a) products ($c_{II}/c_V$) and (b) reactants ($c_{III}/c_{IV}$) species. The current exchange density, $\nabla \cdot \boldsymbol{i}$, is shown in (c). The flow direction has been scaled to 10% of its original size.

the membrane, which exhibits boundary-layer qualities. These large gradients are explained by looking at the current exchange density between the electrolyte and porous electrode phases ($\nabla \cdot \boldsymbol{i}$), which can be seen in Fig. 8(c), and shows the majority of the electrochemical reactions occurring in the vicinity of the membrane.

Using the definition for the power efficiency (30), we plot the efficiency for the full cell as a function of the SOC in Fig. 9. For this calculation, we take the given charge and discharge potentials at a given SOC to calculate a power efficiency at that SOC. The overall power efficiency for a given charge discharge cycle depends on the starting and ending SOCs. As indicated in Fig. 9, the efficiency is slightly higher for the intermediate SOCs. Optimizing the operation of the flow battery requires managing the trade-offs between increased power efficiency and the decrease in capacity associated with not fully converting the vanadium to the desired state. The power efficiencies shown in Fig. 9 do not account for the work associated with pumping the fluid through the electrode; however, the power losses in this cell are minimal. The pumping losses are calculated at $\sim 4 \times 10^{-3}$ W, whereas the electrochemical losses are on the order of 6 W. For cases with higher

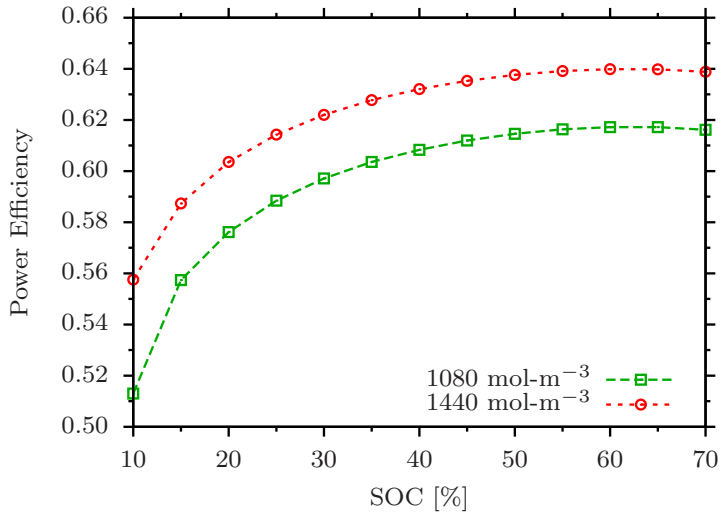


**Figure 9.** Power efficiency for the vanadium cell as a function of SOC.

electrolyte viscosity, increased flow velocities, or reduced permeability of the porous electrodes, pumping losses may not be negligible.

## 3.4 Sensitivity Analysis

Some effort has been made in the literature to use numerical models of flow batteries to study the effects of system design and operating parameters on performance; however, little or no attention has been paid to the sensitivity of the model predictions to the material property inputs into the model [28, 22, 27, 3, 4]. Understanding this sensitivity has two-fold importance: first it can provide insight into the limiting mechanisms affecting performance, and second it can improve confidence in model predictions. The second point is of particular importance for flow battery models because relatively few (or no) experimental measurements are available in the literature for some material properties. In particular, the exchange current density coefficients for the anodic and cathodic reactions are challenging to measure experimentally, and are frequently used as fitting parameters in modeling work [45, 14, 28, 18].

In this work we use the DAKOTA optimization suite [2] to probe our model and determine the sensitivity to various material properties in our VRFB model. We explore the sensitivity of the average charge and discharge voltages, as well as the voltage efficiency with respect to the following properties: $k_1$, $k_2$, $\sigma_s^{eff}$, $D_{II}$, $D_{III}$, $D_{IV}$, $D_V$, $D_{HSO_4^-}$, $D_{SO_4^{2-}}$, $D_{H^+}$. DAKOTA uses Latin Hypercube Sampling (LHS) [2] to determine parameter sets to test and uses Sobol indices to determine the sensitivity of each response value to the specified parameters. Sobol sensitivity indices are the result of a global sensitivity analysis method for determining the impact of the variation in each input on the variation of the output and are widely used for uncertainty quantification [32, 13].

**Table 5.** Means and standard deviations used for sensitivity sampling procedure. All distributions are log-normal.

| Property | Mean | Standard Deviation |
|---|---|---|
| $k_1$ | $1.75 \times 10^{-7}$ | $1.75 \times 10^{-8}$ |
| $k_2$ | $3.0 \times 10^{-9}$ | $3.0 \times 10^{-10}$ |
| $\sigma_s^{eff}$ | 500.0 | 50.0 |
| $D_{II}$ | $2.4 \times 10^{-10}$ | $2.4 \times 10^{-11}$ |
| $D_{III}$ | $2.4 \times 10^{-10}$ | $2.4 \times 10^{-11}$ |
| $D_{IV}$ | $3.9 \times 10^{-10}$ | $3.9 \times 10^{-11}$ |
| $D_V$ | $3.9 \times 10^{-10}$ | $3.9 \times 10^{-11}$ |
| $D_{HSO_4^-}$ | $1.23 \times 10^{-9}$ | $1.23 \times 10^{-10}$ |
| $D_{SO_4^{2-}}$ | $2.2 \times 10^{-10}$ | $2.2 \times 10^{-11}$ |
| $D_{H^+}$ | $9.31 \times 10^{-9}$ | $9.31 \times 10^{-10}$ |

In this work, we sample each material property using a log-normal distribution with a standard deviation of 10% of the mean value. The mean values and corresponding standard deviations are presented in Table 5. A total of 1200 samples were computed and the resulting total Sobol indices are presented in Table 6. The total Sobol indices capture the change in output, in this case the cell voltage, to changes to a given model input including higher-order interactions with other variables.

Based on these sensitivity results, three material properties dominate the simulation results and the resulting cell voltage and efficiency: $k_2$, $D_{H^+}$, and $\sigma_s^{eff}$. The impact of $D_{H^+}$ is unsurprising since it is the dominant factor controlling the polarization across the separator membrane, which is known to be an important factor on flow battery performance. The impact of $k_2$ is high because the $V_4 \leftrightarrow V_5$ reaction is slower than the $V_2 \leftrightarrow V_3$ reaction, and it dominates the reaction overpotential. That said, it is important to note that $k_2$ has few experimental measurements reported in the literature, and the reported value from the work of Gattrell et al. [14] that was used in the model of Shah et al. fits poorly to the experimental data, causing Gattrell et al. to suggest that a simple Butler–Volmer mechanism is insufficient for modeling the reaction kinetics [14, 28]. Some other flow battery modeling work uses $k_2$ as a fitting parameter [18]. Therefore, the high sensitivity of the model results to the value of $k_2$ combined with the significant uncertainty in its estimate must limit confidence in the predictive ability of the model. This result is representative of the important lessons that can be learned from uncertainty quantification studies that have heretofore been neglected in flow battery modeling. The high sensitivity of the model predictions to the carbon felt electronic conductivity $\sigma_s^{eff}$ is also surprising. The conductivity $\sigma_s^{eff}$ is typically orders of magnitude larger than the ionic conductivity of both the anolyte and catholyte and is frequently believed to be less important for improving cell performance. However, because of this large disparity between the ionic and electronic conductivities, the electrochemical reactions tend to occur preferentially near the separator interface and therefore the majority of the current in both the anode and cathode is carried through the carbon felt skeleton. This leads to the high sensitivity to $\sigma_s^{eff}$ that is seen in this analysis.

**Table 6.** Sensitivities of average charge voltage, average discharge voltage, and cycle voltage efficiency on each sampled property. Sensitivities are total Sobol indices.

| Property | Charge Voltage Sensitivity | Discharge Voltage Sensitivity | Voltage Efficiency Sensitivity |
|---|---|---|---|
| $k_1$ | $3.66 \times 10^{-02}$ | $4.29 \times 10^{-02}$ | $4.08 \times 10^{-02}$ |
| $k_2$ | $3.64 \times 10^{-01}$ | $3.40 \times 10^{-01}$ | $3.50 \times 10^{-01}$ |
| $\sigma_s^{eff}$ | $1.91 \times 10^{-01}$ | $1.97 \times 10^{-01}$ | $1.95 \times 10^{-01}$ |
| $D_{II}$ | $2.54 \times 10^{-04}$ | $5.54 \times 10^{-04}$ | $9.78 \times 10^{-05}$ |
| $D_{III}$ | $2.67 \times 10^{-04}$ | $1.37 \times 10^{-03}$ | $8.93 \times 10^{-04}$ |
| $D_{IV}$ | $7.14 \times 10^{-04}$ | $4.36 \times 10^{-03}$ | $2.37 \times 10^{-03}$ |
| $D_V$ | $2.48 \times 10^{-05}$ | $1.38 \times 10^{-02}$ | $5.69 \times 10^{-03}$ |
| $D_{HSO_4^-}$ | $3.10 \times 10^{-03}$ | $5.62 \times 10^{-03}$ | $4.42 \times 10^{-03}$ |
| $D_{SO_4^{2-}}$ | $3.83 \times 10^{-03}$ | $8.04 \times 10^{-03}$ | $5.84 \times 10^{-03}$ |
| $D_{H^+}$ | $3.37 \times 10^{-01}$ | $3.54 \times 10^{-01}$ | $3.48 \times 10^{-01}$ |

## 3.5 Impact of Flow Distribution

In this section, we use the VRFB model to investigate the impact of electrolyte flow configurations on flow battery performance, in particular the impact of open channels adjacent to the porous electrodes for distributing electrolyte. The conclusions drawn here for the VRFB should apply more generally to other flow battery chemistries since the study mainly considers flow configurations. This study is of interest in improving performance in general, but also because several papers discuss the use of serpentine channels, borrowed from fuel cell technology, as conduits for introducing electrolytes to porous electrodes in a flow-by configuration [43, 1, 21]. This configuration is in contrast to a flow-through design, (e.g. [28]), in which the electrolyte is injected directly into the porous electrode. Introducing electrolyte in open channels in contact with the porous electrodes could be beneficial in reducing pumping power for circulation of electrolyte through the flow battery.

### Model with Channels

To facilitate comparison with the flow-through (direct electrode injection) design, we start with the configuration and dimensions of the VRFB discussed in Section 3.3 to validate the numerical model with the results of [28]. Fig. 10 shows the cross section of the three-dimensional model employing open channels, including the grid spacing used. It represents a "unit cell" across the thickness of the full 10 cm × 10 cm electrochemical cell. Hence, this cross section extends for 10 cm into the paper in the three-dimensional model, also shown in Fig. 10. The lateral dimensions are the same as the two-dimensional model shown in Section 3.3. In the present three-dimensional version, 1 mm x 1 mm open channels are cut directly into the collector plates. Only half of the channel is included in the model because of symmetry. The two-dimensional model, without

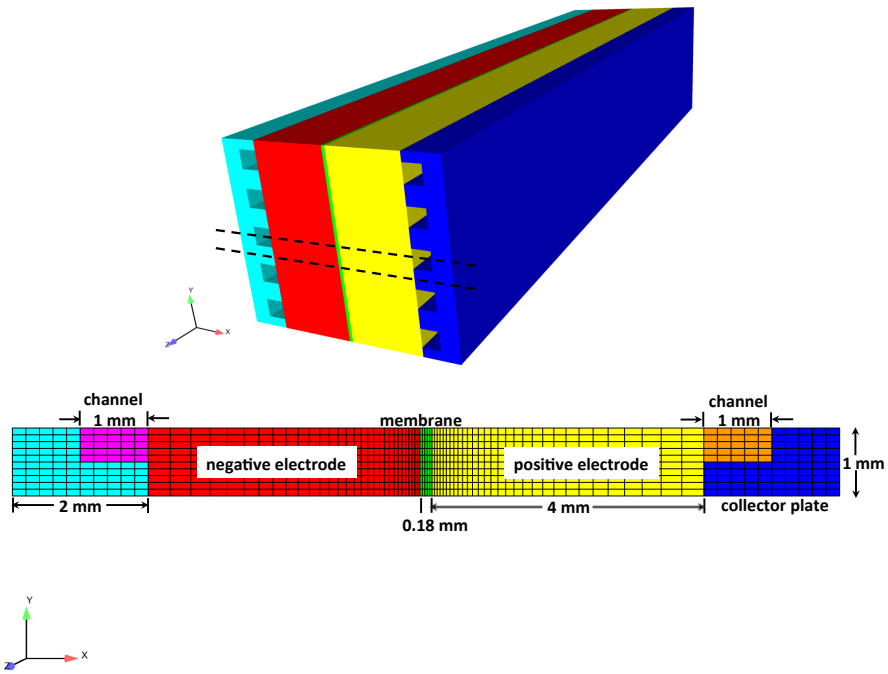


**Figure 10.** Cross section of three-dimensional model employing open channels cut into the collector plates.

channels, can be recovered if the channel volumes are specified as part of the collector plates.

For expediency, flow in the open channels is approximated as flow through porous media. This is equivalent to averaging the Stokes-flow equations over the area of the channels, except that in the following, we treat the effective channel permeability as a parameter. In the model, this allows the flow and transport in the channels to be treated the same as in the porous electrodes, except that in the channels the porous material is not electrochemically active (no transfer currents), and is not electrically conductive. Otherwise, the liquid and species are governed by the same physical mechanisms in the channels as in the porous electrodes.

### Initial and Boundary Conditions

The initial conditions and boundary conditions are completely analogous to those discussed in Section 3.3. In this study the charge and discharge operations are performed separately. Initially the porous electrodes are assumed flooded with the active species for charge ($c_{III}$ and $c_{IV}$) or discharge ($c_{II}$ and $c_V$) at 1080 mol-m$^{-3}$ concentration. For direct injection into the porous electrodes, the electrolyte solution is introduced on the inflow plane by specifying the total flow rate of 1 mL-s$^{-1}$ over the 10 cm $\times$ 4 mm area [28], which is equivalent to the volumetric flux density of the 0.25 cm$^3$/cm$^2$-s. For channel injection, the same flow rate per electrode is introduced over the area

**Table 7.** Flow pressures for 10 cm flow length

| Configuration | Pressure Drop (Pa) |
|---|---|
| Electrode injection | 4567 |
| Channel injection $k_c = 2k_e$ | 2036 |
| Channel injection $k_c = 10k_e$ | 1330 |

of the channels by adjusting the volume flux to account for the reduced cross-sectional area of the channel. The species are introduced by specifying their time dependent concentration as in Section 3.3. On the outflow plane, zero pressure is specified over the electrode areas in the case of electrode injection, or over the channel area with no-flow over the remaining electrode areas for channel injection. The species are allowed to be freely convected out of the simulation domain. The outer surface of the negative collector is specified at zero volts and a constant charging or discharging current density (magnitude 1000 A-m$^{-2}$) is specified uniformly over the outer surface of the positive collector plate. The top and bottom surfaces (constant $y$-coordinate in Fig. 10) are symmetry boundaries.

## Results

Two cases of channel flow are investigated, with the channels modeled using effective channel permeabilities of $k_c = 2k_e$ and $k_c = 10k_e$, where $k_e$ denotes the porous felt electrode permeability ($k_e = 55.3 \times 10^{-11}$ m$^2$). For reference, the effective permeability of an open square channel of dimension $w$ per side is $2.249w^2/64$ (see e.g. [5]). Hence the permeability of the 1 mm × 1 mm channels is $3.51 \times 10^{-8}$ m$^2$. The pressure drop across the length of the cell is shown in Table 7 comparing direct electrode injection with an open flow channel, for the same mass flow rate of 1 mL-s$^{-1}$. Indeed, the channel configuration reduces the pressure requirements by a factor of about 3.5 for the $10k_e$ channel permeability. It should be noted that the pressure drop will not be linear in terms of the channel permeability, because of the flow induced in the porous electrode.

Fig. 11, which shows the streamwise component of velocity across the cell midway between inflow and outflow planes, illustrates the effect of the open channels on the flow distribution. The zero streamwise velocity at zero distance corresponds to the membrane. For direct electrode injection, the flow across the cell is uniform through each electrode, which corresponds to an applied volume flux of 1 mL-s$^{-1}$ over the 10 cm width of the full cell. The large values of streamwise velocity mark the channel locations on the curves for the open channel models. For the same volumetric flow rate, the open channels have a large velocity relative to the velocity in the porous electrodes.

Relative to injecting electrolyte directly into the porous felt electrodes, the introduction of channels detrimentally affects the overall cell potential. Fig. 12 compares the cell potential history, during both charge and discharge, for the two flow configurations. These potentials are not corrected by the 131 mV discussed in [28], which was attributed to portions of the overall cell

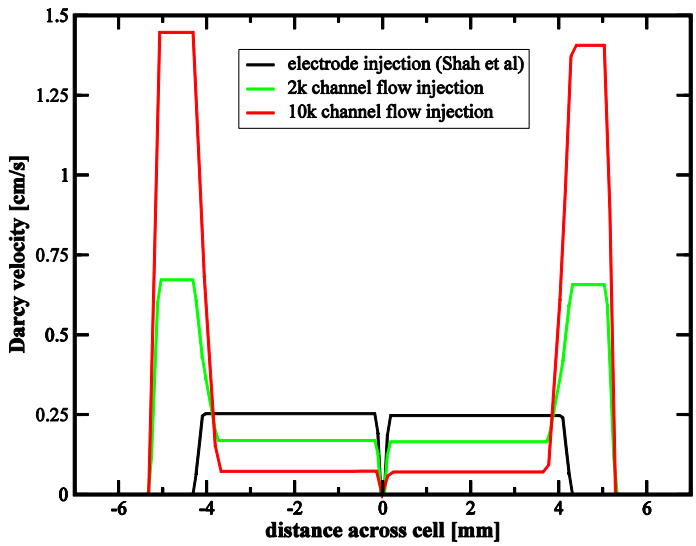


**Figure 11.** Distribution of the streamwise component of Darcy velocity across the thickness of the cell for direct electrode injection and for open channel flow injection, with $k_c = 2k_e$ and $k_c = 10k_e$ permeability ($k_e$ is the electrode felt permeability). The profile intersects the middle of an open channel. All curves correspond to the same volumetric flow rate (1 mL-$s^{-1}$) through the full cell.

impedance not captured in the model. In addition to direct electrode electrolyte injection, the figure shows the cell potential history with the open channels. The $k_c = 2k_e$ channel performs approximately as well as the electrode injection design, showing roughly 10 mV deviation in both charge and discharge curves. However, the $k_c = 10k_e$ channel configuration deviates significantly in flow potential after 30 minutes, corresponding to approximately 70% and 30% SOC, for charge and discharge, respectively. Thus, the open flow channel configuration with high permeability is detrimental to electrochemical performance and limits the operating range of this battery to between 30-70% SOC. This reduced electrochemical performance must be weighed against the reduced pumping energy that channels afford.

The loss of performance can be attributed to electrolyte bypassing the electrodes via the channels. As the battery is charged and the tank concentration of $c_{III}$ is depleted, the flow velocity through the electrodes is too small to support the total applied current of 10 A, which results in the complete depletion of $c_{III}$ in the electrode, as depicted in Fig. 13. The distribution of electrolytes in the cell with high permeability open channels is shown in Fig. 13 at 75% SOC. The ideal distribution of electrolyte would show one-dimensional variation in the cross stream direction and uniform conditions in the streamwise direction, i.e., an injection of infinite flow rate. The electrolyte distribution in the two-dimensional model shown in the verification section indicates the direct electrode injection comes close up to 80% SOC. In the present configuration at 75% SOC, the concentration of $c_{III}$ is depleted, which prevents current transfer further downstream. The open

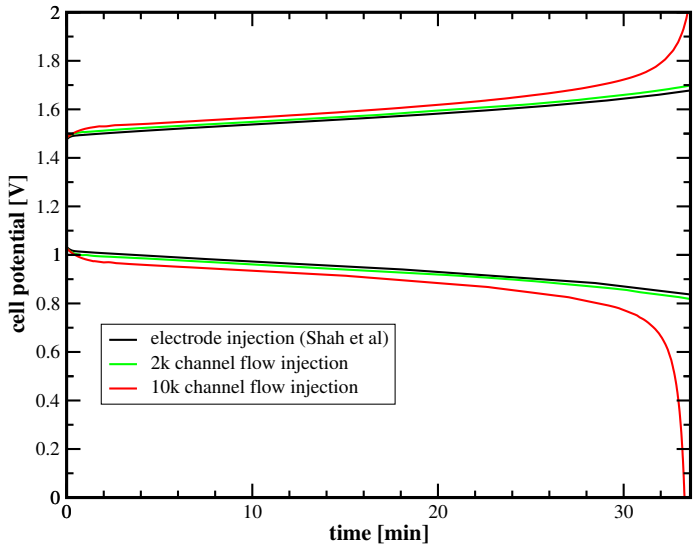


**Figure 12.** Effect of electrolyte flow configuration on cell potential.

channels convect electrolyte downstream past the depletion location, but the cross stream diffusion of vanadium ions is too small to introduce appreciable $c_{III}$ into the electrode. This same depletion occurs on the positive side of the cell involving $c_{IV}$ and $c_V$, and the analogous mechanism occurs in reverse during discharge.

Fig. 14 shows the cross-current density in the electrolyte during a charge cycle for both electrolyte injection configurations at 75% SOC. Similar behavior is noted for discharge. Injection of electrolyte directly into the porous electrodes results in the most uniform current density distribution, but requires the highest pressure gradient. Even at 75% SOC, current transfer occurs along the full length of the cell in the direct-injection configuration. The channel with $k_c = 2k_e$ permeability shows more axial variation, but the performance is acceptable. For the cell with the high-permeability open channel, most of the cross current travels through about half of the cell, coincident with the region where both active species are present in the electrodes (see previous figure). Peak current density in this case is on the order of 1600 A-m$^{-2}$. Similarly, the cross-stream current density in the solid is concentrated near the inflow. Fig. 15 shows the cross stream current density through the solid (collector plates and porous felt) on the inflow cross-section at 50% and 70% SOC. The open channels and the membrane are nonconductive with respect to the solid phase current density. At 50% SOC, with the cell operating satisfactorily, Fig. 15 depicts the nominal distribution of solid current that has to flow around the nonconductive channels, thereby concentrating the current density beneath. At 75% SOC, most of the total cross stream current is concentrated near the inflow region and even higher current densities are depicted, with peak values exceeding 35 mA-cm$^{-2}$.

In summary, this study indicates that channels can reduce pumping pressures while maintaining performance similar to the electrode injection configuration if channels are designed to balance the

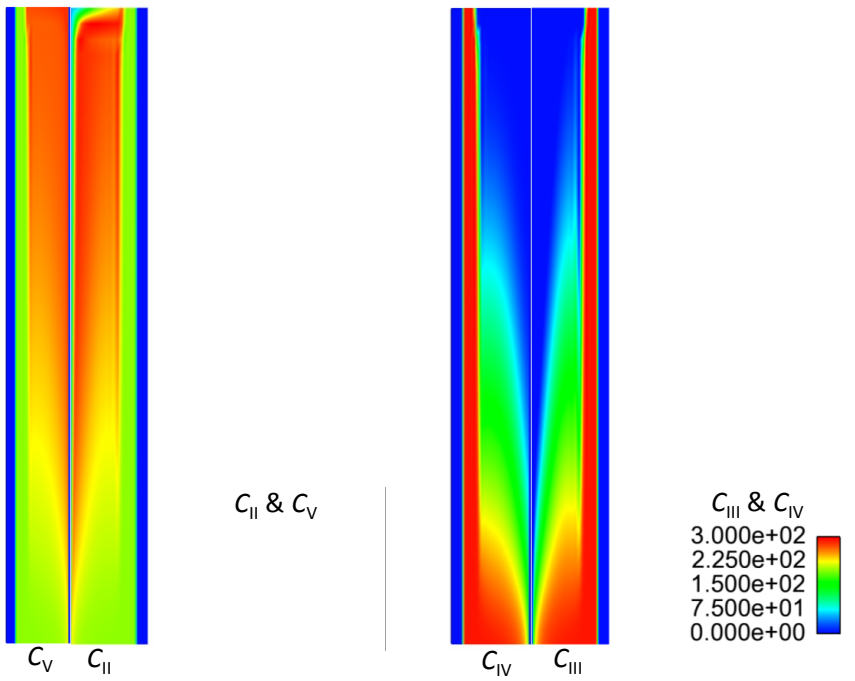


**Figure 13.** Electrolyte concentrations (mol-m$^3$) at 75% SOC during charge for open channel electrolyte injection with 10 $k_e$ channel permeability. In this view, the negative electrode ($c_{II}$ and $c_{III}$) is on the right side, and the positive electrode ($c_{IV}$ and $c_V$) is on the left side. Inflow is from the bottom and outflow at the top. Electrolyte bypassing the porous electrodes via the channels is noted.

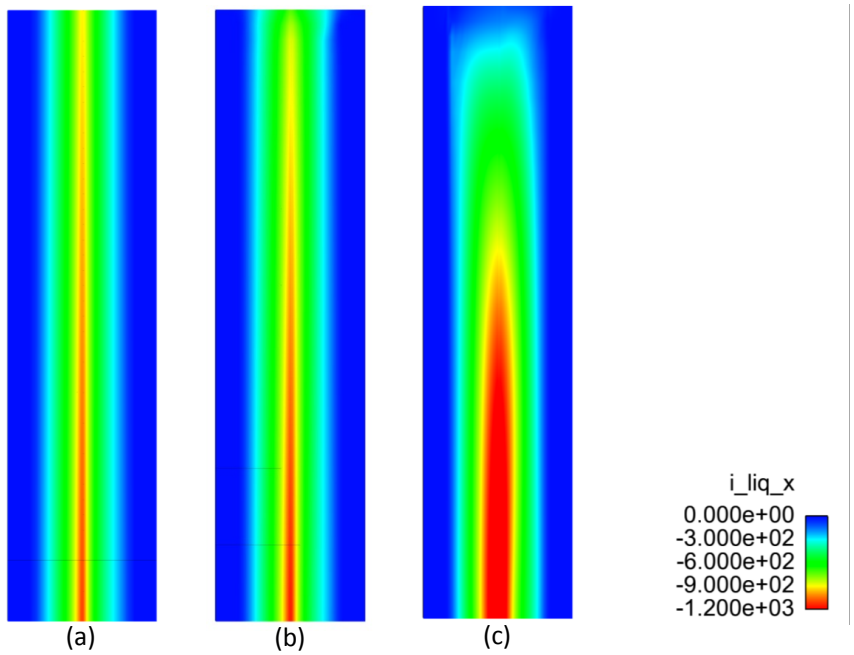


**Figure 14.** Electrolyte cross-current density (A-m$^2$) at about 75% SOC during cell charging for (a) direct electrode injection, and open channel injection with (b) $k_c = 2k_e$ and (c) $k_c = 10k_e$ channel permeability.

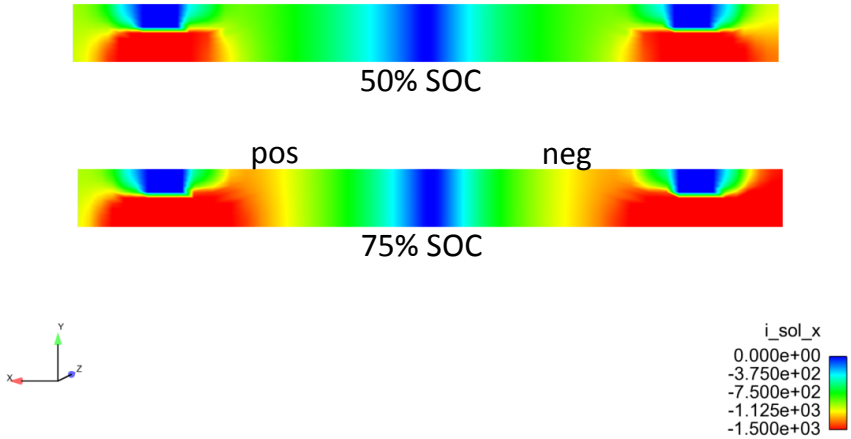


**Figure 15.** Cross-stream current density (A-m$^2$) on the inflow cross section through the solid conductors, including collector plates and porous felt matrix, during charge for the open channel model with 10K permeability.

channel-to-electrode flow ratio not much higher than 4 : 1 based on the results from the $k_c = 2k_e$ channels. Higher flow ratios result in the electrolyte bypassing the electrode via the channels, thus impairing the performance and operating range of the cell. These results hold for the vanadium system, with diffusion coefficients of $2.4 \times 10^{-10}$ m$^2$-s$^{-1}$ for $c_{II}$ and $c_{III}$. Redox species with higher diffusion coefficients may tolerate higher flow channel velocities. In the model with $k_c = 10k_e$ channels, the vanadium ionic flux through the electro-active porous felt electrodes must be supported by diffusion and migration from the channels, both much slower than forced convection. In this case, the electrode thickness becomes important. The time scale for diffusion over a distance $x$ is roughly $t \sim x^2/4D$, where $D$ is the diffusion coefficient. Based on this estimate, $c_{II}$ diffusion across 4 mm and 0.4 mm electrodes takes on the order of 4.6 hours and 167 seconds, respectively. For a given power output, the inlet flux must be sufficient to supply enough reactants to produce the requisite power. Therefore, systems using thinner electrodes must include more electrodes, or use a higher flow rate to prevent the electrode from "starving", i.e., depleting all reactants.

# 4 Conclusion

In this report, we discussed the development of a numerical model to simulate an all vanadium redox flow battery. The simulation included models of the electrochemical reactions using a modified Butler–Volmer form, ion migration in the electrolyte and through the membrane, and current transport via ions as well as conduction in the solid electrode matrix and current collectors. The physical models were based from those described in the work by [28]. The physical models were numerically implemented using the finite element method in the multiphysics code base SIERRA, which is capable of large-scale three-dimensional simulations on parallel supercomputers.

The implementation of the flow battery model neglected some physics, as did the method presented in [28], and serves as a first-pass at modeling a full redox flow cell. The SIERRA infrastructure allows for the easy inclusion of more advanced physical models that could probe the effects of secondary reactions, water transport through the membrane, shunt currents, etc., which could be the focus of future work.

The model, as implemented, was verified using a binary electrolyte test, and a semi-analytical result for a half cell with a fixed concentration profile. Finally a validation was conducted by comparing the simulation results to the experimental results presented in [28]. Subsequently, a sensitivity analysis of the several model parameters was conducted. The findings of that study suggested that the $V_{IV} \leftrightarrow V_V$ reaction, which is slower than the corresponding $V_{II} \leftrightarrow V_{III}$ reaction, is a highly sensitive parameter for predicting the cell potential. Accordingly, the accuracy of this parameter is critical for simulation fidelity and deserves further investigation and modeling. The diffusion coefficient in the membrane is another area that deserves focused investigation. Perhaps the most surprising result is that the model is sensitivity to the electric conductivity of the porous felt.

Lastly, a three-dimensional model of the redox flow cell was investigated in which the electrolyte is delivered to the electrodes via free-flowing channels cut into the collector plates. Such a feature is frequently found in experimental apparatuses, since such features are commonly found in fuel cell collector plates. We showed that such a channel can cause the reactant-rich electrolyte to bypass the porous electrode. The transport of the vanadium ions to the near-membrane area, where much of the reaction occurs, is thus limited by the diffusive process instead of the much faster convective processes that are desired. With some tuning of the pressure drop in the channel, we showed that this effect can be mitigated; however, doing so is only prudent in cases where the pumping losses are high, which was not the case for the cell tested. This study suggests that performance measurements using the serpentine channel may be suboptimal compared with a flow-through design.

# References


[1] D. S. Aaron, Q. Liu, Z. Tang, G. M. Grim, A. B. Papandrew, A. Turhan, T. A. Zawodzinski, and M. M. Mench. Dramatic performance gains in vanadium redox flow batteries through modified cell architecture. *J. Power Sources*, 206:450–3, 2012.

[2] B.M. Adams, L.E. Bauman, W.J. Bohnhoff, K.R. Dalbey, M.S. Ebeida, J.P. Eddy, P.D. Eldred, M.S.and Hough, K.T. Hu, J.D. Jakeman, L.P. Swiler, and D.M. Vigil. Dakota, a multilevel parallel object-oriented framework for design optimization, parameter estimation, uncertainty quantification, and sensitivity analysis: Version 5.3.1 user's manual. Technical Report SAND2010-2183, Sandia, April 2013.

[3] H. Al-Fetlawi, A. A. Shah, and F. C. Walsh. Modelling the effects of oxygen evolution in the all-vanadium redox flow battery. *Electrochim. Acta*, 55(9):3192–205, 2010.

[4] H. Al-Fetlawi, AA Shah, and FC Walsh. Non-isothermal modelling of the all-vanadium redox flow battery. *Electrochim. Acta*, 55(1):78–89, 2009.

[5] R. Berker. Handbuch der physik. *VIII/2, Springer-Verlag, Berlin*, 74, 1963.

[6] D. M. Bernardi and M. W. Verbrugge. Mathematical model of a gas diffusion electrode bonded to a polymer electrolyte. *AIChE journal*, 37(8):1151–63, 1991.

[7] D. M. Bernardi and M. W. Verbrugge. A mathematical model of the solid-polymer-electrolyte fuel cell. *J. Electrochem. Soc.*, 139:2477, 1992.

[8] A. N. Brooks and T. J. R. Hughes. Streamline upwind/Petrov-Galerkin formulations for convection dominated flows with particular emphasis on the incompressible Navier-Stokes equations. *Comput. Method. Appl. M.*, 32(1):199–259, 1982.

[9] C. P. de Leon, A. Frias-Ferrer, J. Gonzalez-Garcia, D. A. Szanto, and F. C. Walsh. Redox flow cells for energy conversion. *J. Power Sources*, 160(1):716–32, 2006.

[10] K. C. Divya and J. Østergaard. Battery energy storage technology for power systems—An overview. *Electr. Pow. Syst. Res.*, 79(4):511–20, 2009.

[11] C. Fabjan, J. Garche, B. Harrer, L. Jörissen, C. Kolbeck, F. Philippi, G. Tomazic, and F. Wagner. The vanadium redox-battery: an efficient storage unit for photovoltaic systems. *Electrochim. Acta*, 47(5):825–31, 2001.

[12] C. Fujimoto, S. Kim, R. Stains, X. Wei, L. Li, and Z. G. Yang. Vanadium redox flow battery efficiency and durability studies of sulfonated diels alder poly (phenylene) s. *Electrochem. Commun.*, 20:48–51, 2012.

[13] Graham G. and Kristin I. Estimating Sobol sensitivity indices using correlations. *Environ. Modell. Softw.*, 37(0):157–66, 2012.

[14] M. Gattrell, J. Park, B. MacDougall, J. Apte, S. McCarthy, and C. W. Wu. Study of the mechanism of the vanadium 4+/5+ redox reaction in acidic solutions. *J. Electrochem. Soc.*, 151(1):123–30, 2004.

[15] M. A. Heroux, R. A. Bartlett, V. E. Howle, R. J. Hoekstra, J. J. Hu, T. G. Kolda, R. B. Lehoucq, K. R. Long, R. P. Pawlowski, E. T. Phipps, et al. An overview of the trilinos project. *ACM Transactions on Mathematical Software (TOMS)*, 31(3):397–423, 2005.

[16] C. Jia, J.o Liu, and C. Yan. A significantly improved membrane for vanadium redox flow battery. *J. Power Sources*, 195(13):4380–83, 2010.

[17] M. Kazacos and M. Skyllas-Kazacos. Performance characteristics of carbon plastic electrodes in the all-vanadium redox cell. *J. Electrochem. Soc.*, 136(9):2759–60, 1989.

[18] K. W. Knehr, E. Agar, C. R. Dennison, A. R. Kalidindi, and E. C. Kumbur. A transient vanadium flow battery model incorporating vanadium crossover and water transport through the membrane. *J. Electrochem. Soc.*, 159(9):A1446–A1459, 2012.

[19] M. Li and T. Hikihara. A coupled dynamical model of redox flow battery based on chemical reaction, fluid flow, and electrical circuit. *IEICE Trans. Fundamentals*, E91-A(7):1741–47, 2008.

[20] Y.-H. Li and S. Gregory. Diffusion of ions in sea water and in deep-sea sediments. *Geochem. Cosmochim. Ac.*, 38(5):703–14, 1974.

[21] Q. H. Liu, G. M. Grim, A. B. Papandrew, A. Turhan, T. A. Zawodzinski, and M. M. Mench. High performance vanadium redox flow batteries with optimized electrode configuration and membrane selection. *J. Electrochem. Soc.*, 159(8):A1246–A1252, 2012.

[22] X. Ma, H. Zhang, and F. Xing. A three-dimensional model for negative half cell of the vanadium redox flow battery. *Electrochim. Acta*, 58:238–46, 2011.

[23] J. Newman and K. E. Thomas-Alyea. *Electrochemical Systems*. John Wiley & Sons, Hoboken, New Jersey, 3rd edition, 2004.

[24] P. K. Notz, S. R. Subia, M. M. Hopkins, H. K. Moffat, and D. R. Noble. Aria 1.5: User Manual. SAND2007-2734, 2007.

[25] S. Olson and R. W. III. Fri. *The National Academies Summit on America's Energy Future: Summary of a Meeting*. The National Academies Press, Washington, DC, 2008.

[26] M. Pourbaix. *Atlas of electrochemical equilibria in aqueous solutions*. National Association of Corrosion Engineers, 1974.

[27] A. A. Shah, H. Al-Fetlawi, and F. C. Walsh. Dynamic modelling of hydrogen evolution effects in the all-vanadium redox flow battery. *Electrochim. Acta*, 55(3):1125–39, 2010.

[28] A. A. Shah, M. J. Watt-Smith, and F. C. Walsh. A dynamic performance model for redox-flow batteries involving soluble species. *Electrochim. Acta*, 53(27):8087–100, 2008.

[29] M. Skyllas-Kazacos, M. H. Chakrabarti, S. A. Hajimolana, F. S. Mjalli, and M. Saleem. Progress in flow battery research and development. *J. Electrochem. Soc.*, 158(8):R55–R79, 2011.

[30] M. Skyllas-Kazacos and L. Goh. Modeling of vanadium ion diffusion across the ion exchange membrane in the vanadium redox battery. *Journal of Membrane Science*, 399–400:43–8, 2012.

[31] M. Skyllas-Kazacos, M. Rychcik, R. G. Robins, A. G. Fane, and M. A. Green. New all-vanadium redox flow cell. *J. Electrochem. Soc.*, 133(5):1057–58, 1986.

[32] I. M. Sobol. Global sensitivity indices for nonlinear mathematical models and their Monte Carlo estimates. *Math. Comput. Simulat.*, 55(1–3):271 – 280, 2001.

[33] E. Sum, M. Rychcik, and M. Skyllas-Kazacos. Investigation of the V(V)/V(IV) system for use in the positive half-cell of a redox battery. *J. Power Sources*, 16(2):85–95, 1985.

[34] E. Sum and M. Skyllas-Kazacos. A study of the V(II)/V(III) redox couple for redox flow cell applications. *J. Power Sources*, 15(2):179–90, 1985.

[35] B. Sun and M. Skyllas-Kazacos. Chemical modification of graphite electrode materials for vanadium redox flow battery application—Part II. Acid treatments. *Electrochim. Acta*, 37(13):2459–65, 1992.

[36] B. Sun and M. Skyllas-Kazacos. Modification of graphite electrode materials for vanadium redox flow battery application—I. Thermal treatment. *Electrochim. acta*, 37(7):1253–60, 1992.

[37] A. Tang, J. Bao, and M. Skyllas-Kazacos. Dynamic modelling of the effects of ion diffusion and side reactions on the capacity loss for vanadium redox flow battery. *J. Power Sources*, 196(24):10737–47, 2011.

[38] U.S. Deptartment of Energy, Office of Electricity Delivery and Energy Reliability. Advanced materials and devices for stationary electrical energy application, 2010. http://energy.gov/sites/prod/files/oeprod/DocumentsandMedia/AdvancedMaterials_12-30-10_FINAL_lowres.pdf, accessed August 22, 2013.

[39] U.S. Deptartment of Energy, Office of Electricity Delivery and Energy Reliability. Electric power industry needs for grid-scale storage applications, 2010. http://energy.gov/sites/prod/files/oeprod/DocumentsandMedia/Utility_12-30-10_FINAL_lowres.pdf, accessed Sept. 9, 2013.

[40] M. W. Verbrugge and R. F. Hill. Ion and solvent transport in ion-exchange membranes I. A macrohomogeneous mathematical model. *J. Electrochem. Soc.*, 137(3):886–93, 1990.

[41] M. Vynnycky. Analysis of a model for the operation of a vanadium redox battery. *Energy*, 36(4):2242–56, 2011.

[42] W. Wang, Q. Luo, B. Li, X. Wei, L. Li, and Z. G. Yang. Recent progress in redox flow battery research and development. *Adv. Funct. Mater.*, 23(8):970–86, 2012.

[43] A. Z. Weber, M. M. Mench, J. P. Meyers, P. N. Ross, J. T. Gostick, and Q. Liu. Redox flow batteries: a review. *J. Appl. Electrochem.*, 41(10):1137–64, 2011.

[44] J. Xi, Z. Wu, X. Qiu, and L. Chen. Nafion/SiO2 hybrid membrane for vanadium redox flow battery. *J. Power Sources*, 166(2):531–6, 2007.

[45] T. Yamamura, N. Watanabe, T. Yano, and Y. Shiokawa. Electron-Transfer Kinetics of $Np^{3+}/Np^{4+}$, $NpO_2^+/NpO_2^{2+}$, $V^{2+}/V^{3+}$, and $VO^{2+}/VO_2^+$ at carbon electrodes. *J. Electrochem. Soc.*, 152(4):830–6, 2005.

[46] D. You, H. Zhang, and J. Chen. A simple model for the vanadium redox battery. *Electrochim. Acta*, 54(27):6827–36, 2009.

[47] G. E. Zaikov, A. L. Iordanskii, and V. S. Markin. *Diffusion of electrolytes in polymers*. VSP BV, 1988.

# DISTRIBUTION:

1 Dr. Imre Gyuk (electronic copy)
U.S. Department of Energy
Office of Electricity Delivery and Energy Reliability
OE-10/Forrestal Building
1000 Independence Ave., S.W.
Washington DC 20585
imre.gyuk@bq.doe.gov

1 Dr. Z. (Gary) Yang (electronic copy)
UniEnergy Technologies
4333 Harbour Pointe Blvd. S.W., Suite A
Mukilteo, WA 98275
gary-yang@uetechnologies.com

1 Dr. S. Hickey (electronic copy)
Redflow Ltd.
27 Counihan Rd.
Seventeen Mile Rocks
Brisbane Qld 4073 Australia
steven.hickey@redflow.com

1 Soowhan Kim (electronic copy)
PNNL
902 Battelle Blvd.
PO Box 999, MSIN K2-03
Richland, WA 99342
soowhan.kim@pnl.gov

1 Dr. Rick Winter (electronic copy)
Primus Power
39967 Trustway
Hayward, CA 94545
rick.winter@primuspower.com

1 Dr. T. Zawodzinski (electronic copy)
Univ. of Tennessee, Knoxville
Dept. of Chemical & Biomolecular Engineering
442 Dougherty Hall
Knoxville, TN 37996
tzawodzi@utk.edu

1 Dr. J. S. Wainright (electronic copy)
Case Western Reserve University
Dept. of Chemical Engineering
10900 Euclid Ave.
Cleveland, OH 44106-7217
jsw7@case.edu

| | | |
|---|---|---|
| 1 | MS 0613 | T. M. Anderson, 2546 (electronic copy) |
| 1 | MS 0613 | S. R. Ferreira, 2546 (electronic copy) |
| 1 | MS 0613 | N. Hudak, 2546 (electronic copy) |
| 1 | MS 0613 | D. Ingersoll, 2546 (electronic copy) |
| 1 | MS 0613 | T. F. Wunsch, 2546 (electronic copy) |
| 1 | MS 0815 | J. E. Johannes, 1500 (electronic copy) |
| 1 | MS 0828 | R. B. Bond, 1541 (electronic copy) |
| 1 | MS 0828 | J. R. Clausen, 1513 (electronic copy) |
| 1 | MS 0828 | S. N. Kempka, 1510 (electronic copy) |
| 1 | MS 0836 | M. J. Martinez, 1513 (electronic copy) |
| 1 | MS 0836 | H. K. Moffat, 1516 (electronic copy) |
| 1 | MS 0840 | D. J. Rader, 1513 (electronic copy) |
| 1 | MS 0885 | T. L. Aselage, 1810 (electronic copy) |
| 1 | MS 0888 | C. Fujimoto, 1834 (electronic copy) |
| 1 | MS 9957 | G. J. Wagner , 8365 (electronic copy) |
| 1 | MS 9957 | V. E. Brunini, 8365 (electronic copy) |
| 1 | MS 1108 | S. J. Hearne, 6111 (electronic copy) |
| 1 | MS 0899 | Technical Library, 9536 (electronic copy) |

This page intentionally left blank.

Sandia National Laboratories